



with Cu K α radiation (45 kV and 40 mA, 20–80° 2 θ range, a virtual step scan of 0.0263° 2 θ and virtual time per step of 200 s). Full QPA analyses were assessed using the combined Rietveld and reference intensity ratio (RIR) methods: 10 wt% corundum (NIST SRM 676a) was added to the sample, and treated as an additional phase in the refinements.^{10,15} Instrumental contribution, was evaluated by means of the NIST SRM 660b standard (LaB $_6$), and taken into account in the refinements. Rietveld refinements were carried out by means of GSAS-EXPGUI software packages.^{16,17} Microstructure of the received **K7000** was solved through the whole powder pattern modelling (WPPM),^{18,19} as implemented in the PM2K software package.²⁰ The WPPM formalism allows us to describe each observed peak profile as a convolution of instrumental and sample-related physical effects, and refining the corresponding model parameters directly on the observed data. For this purpose, aiming at handling data with a high signal/noise ratio were employed, collected using the same instrument and set-up described above, but in the 20–115° 2 θ range, with a virtual step of 0.1° 2 θ , and virtual time per step of 500 s. The instrumental contribution was obtained by parameterising the profile of 14 *hkl* reflections from the NIST SRM 660b standard (LaB $_6$), according to the Caglioti *et al.* relationship.²¹ Crystalline domains were approximated to be spherical and their diameter distributed according to a lognormal curve.

Optical properties of the specimen were analysed *via* diffuse reflectance spectroscopy (DRS), performed using a Shimadzu UV 3100 (JP) spectrometer, equipped with a BaSO $_4$ integrating sphere. Spectra of the samples were acquired in the UV-Vis range (250–750 nm) with 0.2 nm resolution, with BaSO $_4$ as reference. Raman spectroscopy was also assessed; spectra were acquired in the 50–1000 cm $^{-1}$ wavenumber range, with 4 cm $^{-1}$ resolution, on a Bruker RFS 100/S (DE), equipped with a Nd:YAG laser (1064 nm) as the excitation source. FT-IR was performed with the aim of detecting the occurrence of OH groups and/or water adsorbed on the photocatalyst surface. This was carried out on a Bruker Tensor 27 (DE) spectrometer. The measurements were carried out over the wavenumber range of 4000–350 cm $^{-1}$, in attenuated total reflectance (ATR) mode.

X-ray photoelectron spectroscopy (XPS) was used to characterise the elemental composition of the sample and the chemical state of the titanium, oxygen and carbon species. XPS spectra were acquired in an Ultra High Vacuum (UHV) system with a base pressure of 2×10^{-10} mbar. The system is equipped with a hemispherical electron energy analyser (SPECS Phoibos 150), a delay-line detector and a monochromatic AlK α (1486.74 eV) X-ray source. High resolution spectra were recorded at normal emission take-off angle and with a pass-energy of 20 eV, which provides an overall instrumental peak broadening slightly better than 0.5 eV. For XPS measurements the sample was diluted in Milli-Q water and a thin film was deposited on silicon by drop coating. Ar $^{+}$ ion sputtering at 2 kV was used to remove the surface adsorbed species and access to the subsurface region for comparison. The resulting XPS spectra were calibrated in binding energy by referencing to the C 1s peak from contamination at 284.8 eV.

PCA tests were assessed in the gas–solid phase, monitoring the degradation of NO $_x$. The reactor used has been described in detail elsewhere.^{10,22,23} The initial concentration of NO $_x$ (kept stable throughout the experiments, and prepared using synthetic air and NO $_x$ gas) was 0.2 ppm. Two mass flow controllers were used to prepare the mixture of air with the desired concentration of NO $_x$, with a flow rate of 1 L min $^{-1}$; this initial step was necessary to ensure the sample saturation, and ensuring that during the test, measurement of NO $_x$ is exclusively due to the photocatalytic process (*i.e.* no absorption from the sample, nor from the reactor walls).²⁴ The outlet concentration of NO $_x$ was measured using a chemiluminescence analyser (AC-30 M, Environment SA, FR).

Samples were prepared in the form of a thin layer of powder, with a constant mass (~0.10 g), and thus approximately constant thickness, in a 6 cm diameter Petri dish. Tests were performed at 18.1 ± 1 °C (temperature inside the reactor) with a relative humidity of 31%. These parameters, controlled by means of a thermocouple that was placed inside the chamber, and a humidity sensor placed in the inlet pipe, remained stable throughout the tests. The light source employed was a LED white light, irradiating only in the visible region (Philips LED Bulb Warm white), placed 28 cm from the photocatalyst, and the light intensity reaching the photocatalyst was 7 W m $^{-2}$ in the visible range – being nil in the UVA (its emission spectrum being reported in the ESI, Fig. S1†). Once the desired concentration of NO $_x$ was attained, the window glass was uncovered, the LED white-lamp turned on, and the PCA reaction started. PCA tests were repeated in triplicate, using the very same sample and with the same protocol of the first test, so as to check the repeatability, recyclability and photostability of the **K7000** batches.

Results and discussion

X-ray analysis

QPA data are shown in Table 1; a representative output of a Rietveld refinement is depicted in Fig. S2.† Rietveld–RIR data showed **K7000** to consist of anatase as the only crystalline phase, for all three batches examined. Also, all three batches were shown to have a low amount of amorphous phase, varying

Table 1 Rietveld agreement factors, and phase composition of **K7000** TiO $_2$. The phase composition was calculated from the Rietveld refinements of X-ray diffraction patterns, using the NIST 676a internal standard^a

| K7000, batch | No of variables | Agreement factors | | | Phase composition (wt%) | |
|--------------|-----------------|-------------------|--------------|----------|-------------------------|---------------|
| | | $R_{(F^2)}$ (%) | R_{wp} (%) | χ^2 | Anatase | Amorphous |
| 1 | 15 | 3.74 | 4.79 | 2.24 | 91.9 \pm 1.3 | 8.1 \pm 1.3 |
| 2 | 15 | 3.56 | 4.31 | 1.98 | 93.5 \pm 1.1 | 6.5 \pm 1.1 |
| 3 | 15 | 3.56 | 4.66 | 2.18 | 93.1 \pm 1.2 | 6.9 \pm 1.2 |

^a Note: there were 2285 observations; the number of anatase reflections in the data set was 32.

from 6.5 to 8.1 wt%, depending from the batch used. In any case, the actual mineralogical composition was very close in all the three batches. By contrast, we have previously shown that P25 is composed of only 76.3 wt% anatase, with 10.6 wt% rutile, and 13.0 wt% amorphous phase.¹²

Individual microstructural analysis and size distribution for the anatase phase present in the three batches of K7000 are shown in Fig. 1a–c and Table 2; a graphical output of the WPPM modelling is shown in Fig. 1a. From this novel XRD analysis, the anatase average crystalline domain diameters were found to be in the range of 2.3–3.3 nm (with a very narrow size distribution for all three batches, the mode being 2.0 nm in all cases, *cf.* Table 2). Moreover, in all three probability distributions, the right-hand tail is longer than the left, implying that those distributions are skewed to the right (*i.e.* positive skewness). Thus – assuming a unimodal model for the lognormal size distribution – all the three batches exhibited very similar microstructural characteristics. However, as can be seen in

Fig. 1a, in assuming a unimodal model we do not obtain a perfect fit: some features are still present in the difference curve (continuous blue line in Fig. 1a), likely due to a non-ideal distribution of crystalline domains. For this reason, HR-TEM analysis was carried out, to obtain evidence endorsing this suspected non-ideal domain size distribution, *cf.* Fig. 2a–d. As can be clearly seen in Fig. 2a–d, K7000 shows the simultaneous presence of small and large domains – the small crystalline domains being much more strongly aggregated, *cf.* Fig. 2a and b. Therefore, the WPPM analysis was performed a second time, considering a bimodal size distribution for anatase. As can be seen in Fig. 1a, the bimodal model led to an almost perfect fit, the resulting difference curve virtually being a straight line (continuous dark grey line in Fig. 1a). Quantitative results of the bimodal size distribution model are depicted in Table 3; introducing a second fraction does not change the unit cell parameter results (sizes and volume are unaltered). As for the domain size, we observe the appearance of a small quantity of

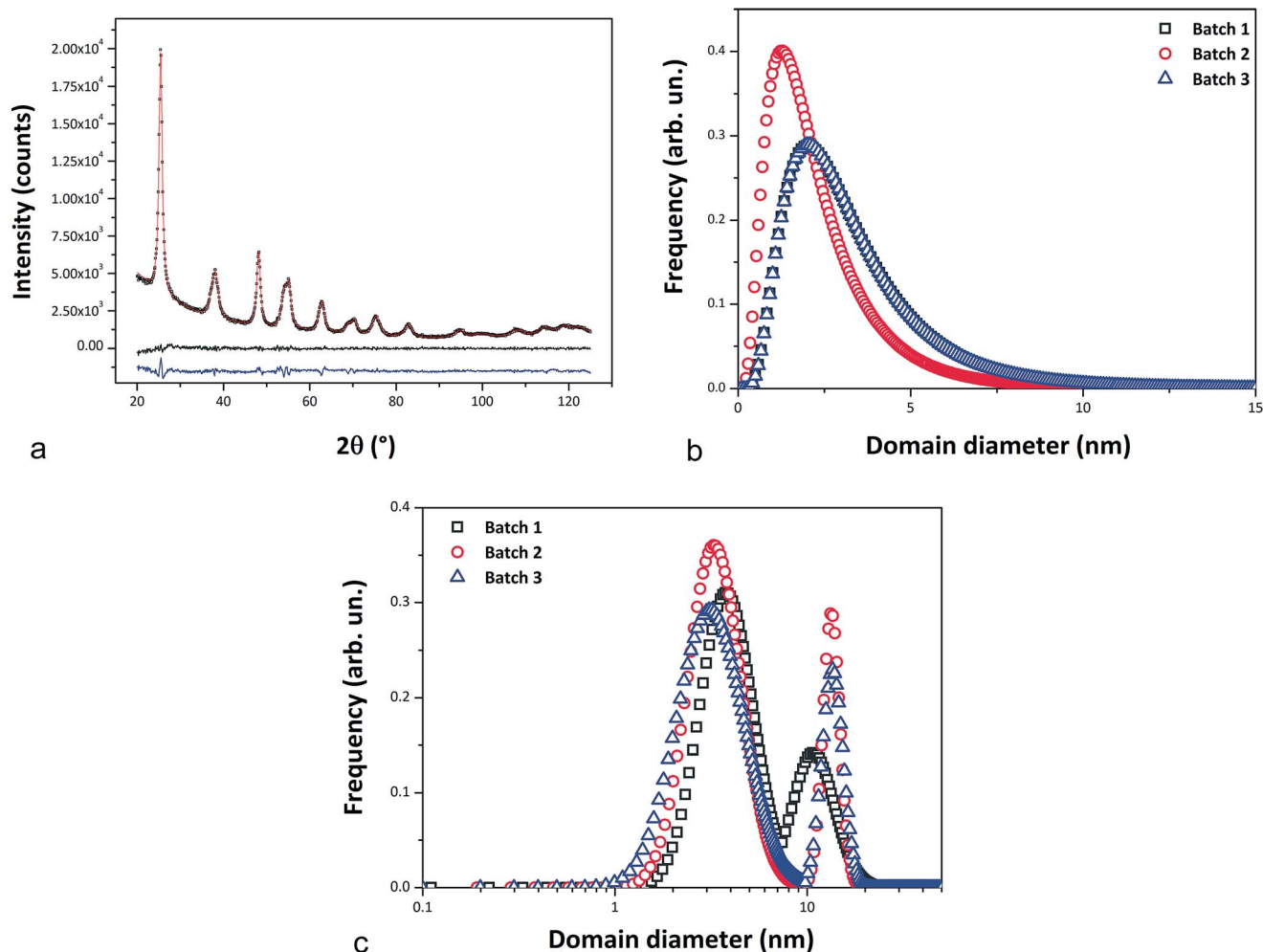


Fig. 1 (a) WPPM output of the K7000 (batch 1) specimen. The red line represents the calculated pattern and the black open squares the measured one. The dark grey (upper) and blue (lower) continuous lines at the bottom are the difference curves between observed and calculated profiles, for the proposed bimodal and unimodal size distribution models, respectively. (b) Crystalline domain size distributions for the anatase phase in K7000, assuming a unimodal model. (c) Bimodal size distribution for anatase (size reported in log-scale), as obtained from the WPPM analysis.

Table 2 WPPM agreement factors, unit cell parameters, average crystalline domain diameter and skewness of K7000, using the unimodal model

| K7000, batch | Agreement factors | | | Unit cell parameters | | | | Mean crystalline domain diameter (nm) | Skewness of the size distribution (nm) |
|--------------|-------------------|---------------|----------|----------------------|-----------|----------|------------------------|---------------------------------------|--|
| | R_{wp} (%) | R_{exp} (%) | χ^2 | a | b (nm) | c (nm) | V (nm ³) | | |
| 1 | 4.04 | 2.33 | 1.74 | 0.3793(1) | 0.9524(1) | 0.137(1) | 3.3 ± 0.1 | 2.1 ± 0.1 | |
| 2 | 4.87 | 2.28 | 2.15 | 0.3792(1) | 0.9519(1) | 0.137(1) | 2.3 ± 0.1 | 2.5 ± 0.1 | |
| 3 | 3.82 | 2.27 | 1.68 | 0.3792(1) | 0.9526(1) | 0.137(1) | 3.3 ± 0.1 | 2.1 ± 0.1 | |

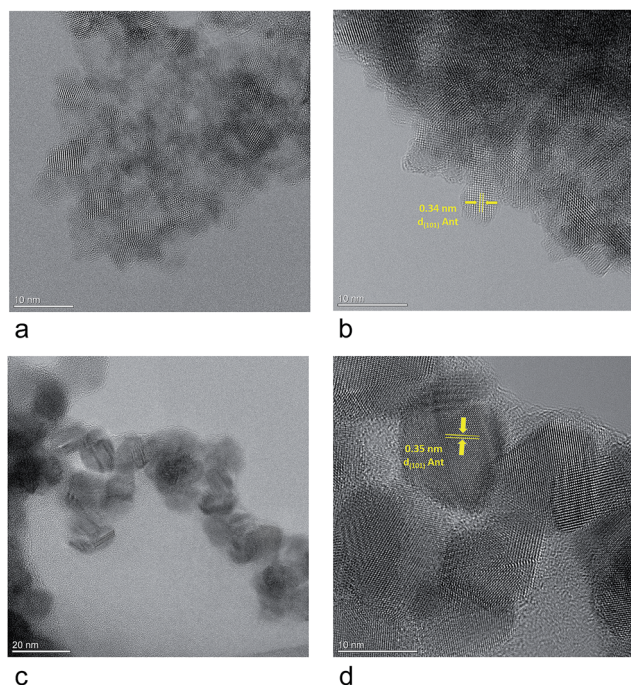


Fig. 2 (a) HR-TEM micrograph of K7000, showing small anatase crystalline domains. (b) HR-TEM micrograph of K7000, showing small anatase crystalline domains. The $d_{(101)}$ crystallographic planes of anatase are shown. (c) HR-TEM micrograph of K7000, showing larger anatase crystalline domains. (d) HR-TEM micrograph of K7000, showing larger anatase crystalline domains. The $d_{(101)}$ crystallographic planes of anatase are also shown.

a second, larger-sized fraction of anatase (11.9–15.5 nm, Fig. 2c and d), co-existing with the smaller 3.8–4.4 nm domains. Hence, this extra fraction of material is able to explain the presence of the long tail in the actual distribution leading towards anatase larger sizes.

Data obtained are thus only partially consistent with those reported by Quesada-Cabrera *et al.*, who stated that K7000 had a “crystallite” size of around 15 nm, obtained using the Scherrer equation, and with a titania content of roughly 95% (though they did not specify whether that remaining 5% was amorphous or not).²⁵ Consequently, they neglected the fraction of the small anatase crystalline domains below 5 nm diameter. In this regard, it is noteworthy that diffraction is sensitive to the volume, therefore to the fraction in that volume, which is the dominant one. A “crystallite” size of ~15 nm is also given in the data sheet of K7000 manufacturer, though they state a TiO₂ content of >87.5%.²⁶

Spectroscopic analyses

DRS spectrum of K7000 is given in Fig. 3, showing an absorption in the visible range. In nitrogen doped TiO₂, this absorption is generally attributed to mid-gap states located just above the valence band.^{27,28} However, in this particular case, an organic carbon complex is attached to the surface of these TiO₂ nanoparticles (NPs), rather than being accommodated in TiO₂ lattice. This explains the observed absorption in the visible region – *cf.* XPS analysis. The optical band gap (E_g) of K7000 was also calculated, taking advantage of the Tauc plot. DRS experimental data were converted to the absorption coefficient α via the Kubelka–Munk equation. The absorption edge of a semiconductor can thus be expressed as: $(\alpha h\nu)^{1/\gamma} = A(h\nu - E_g)$. In this, A is a material constant, h is Planck’s constant, ν is the frequency of the light, E_g is the energy band gap of allowed transitions, and the power coefficient γ is characteristic of the type of transition. For TiO₂ nanoscale semiconductor materials, the value of γ is accepted to be equal to 2, since for such materials, the transition is assumed to be indirectly allowed.²⁹ Hence, if we plot $(\alpha h\nu)^{0.5}$ against $h\nu$, we obtain the energy band gap of the semiconductor material (inset of Fig. 3) from the x -axis ($\alpha = 0$) intercept of the line tangent to the inflection point of the

Table 3 WPPM agreement factors, unit cell volumes, and average crystalline domain diameter of K7000, using the proposed bimodal model

| K7000, batch | Agreement factors | | | Anatase 1 | | Anatase 2 | |
|--------------|-------------------|---------------|----------|---------------------------|-------------------|---------------------------|-------------------|
| | R_{wp} (%) | R_{exp} (%) | χ^2 | Volume (nm ³) | Average size (nm) | Volume (nm ³) | Average size (nm) |
| 1 | 3.08 | 2.28 | 1.35 | 0.137(1) | 4.4 ± 0.3 | 0.136(1) | 11.9 ± 0.6 |
| 2 | 3.98 | 2.23 | 1.78 | 0.137(1) | 3.8 ± 0.1 | 0.137(1) | 13.6 ± 0.5 |
| 3 | 4.24 | 2.23 | 1.90 | 0.137(1) | 4.0 ± 0.2 | 0.136(1) | 15.5 ± 0.8 |

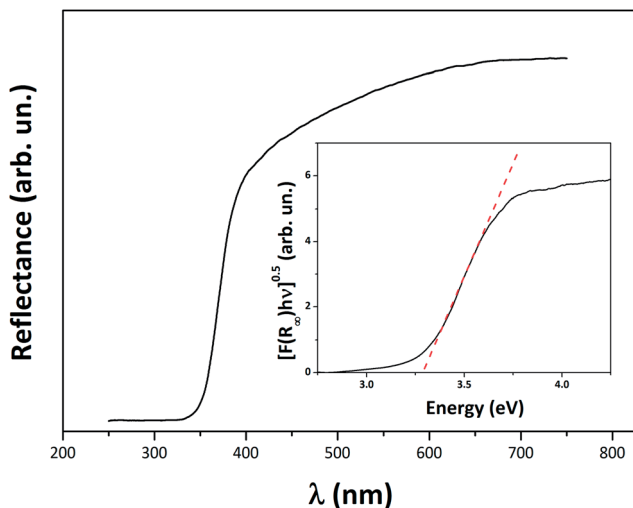


Fig. 3 UV-Vis spectrum of K7000; in the inset is reported the Kubelka Munk elaboration versus energy for K7000. The dashed red line represents the x-axis intercept of the line that is tangent to the inflection point of the curve for K7000 (apparent optical E_g) calculated using the Tauc procedure.

curve. Optical E_g of K7000 was found to be 3.30 ± 0.01 eV, thus in line with the expected value for anatase.⁸

Raman spectroscopy confirmed the XRD results: only Raman modes assignable to anatase were detected in the K7000 spectrum (Fig. S3†). Moreover, the smaller crystalline domain size of anatase in K7000, compared to that in P25, is also confirmed by analysing and comparing the position and full width at half maximum (FWHM) of the symmetric vibrational E_g (O–Ti–O) Raman mode of anatase in K7000 versus P25. The obtained position of the Raman E_g mode in K7000 (147.7 cm^{-1}) is obviously blue shifted compared to that of anatase in P25 (142.7 cm^{-1} , dotted line in the inset of Fig. S3†); the FWHM of K7000 Raman E_g mode (18.7 cm^{-1}) is broader than that of anatase in P25 (11.5 cm^{-1}). This confirms not only the smaller crystalline domain size of K7000 vs. P25, but also its higher disorder.³⁰

An FT-IR spectrum is reported in Fig. S4.† The huge broad band, centred at approximately 3425 cm^{-1} , is assigned to surface-adsorbed hydroxyl groups (this being an advantage for PCA),³¹ whilst the peak at around 1630 cm^{-1} corresponds to the bending vibrations of O–H; the band in the range of $400\text{--}600 \text{ cm}^{-1}$ clearly belongs to Ti–O–Ti vibrations.

XPS analysis

Fig. 4 shows high resolution XPS spectra obtained for Ti 2p (a), O 1s (b) and C 1s (c) core levels of K7000, after a soft etching with argon ions. Furthermore, the best fits are also included for the O 1s and C 1s core levels.

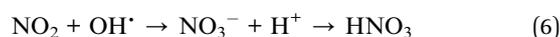
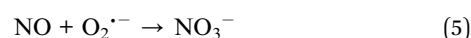
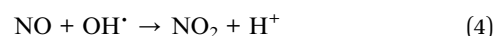
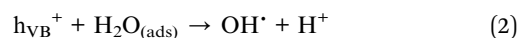
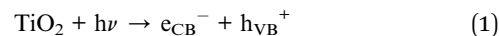
Two main features dominate the Ti 2p spectrum, appearing at binding energies (BE) of (458.8 ± 0.1) eV and (464.6 ± 0.1) eV, that correspond to Ti 2p_{3/2} and Ti 2p_{1/2}, respectively. These values are in good agreement with previously reported BEs for TiO₂ NPs.³² Consequently, a main component is observed in the O 1s region at (530.1 ± 0.1) eV and ascribed to the oxygen atoms of the TiO₂ NPs.³² The relatively small component that appears at (531.3 ± 0.1)

eV is usually assigned to adsorbed surface species such as hydroxyl groups,³³ and/or carbonate-like species in carbon-doped TiO₂ samples. On the other hand, in the case of the C 1s core level, three components were necessary for the fitting of the spectrum. The first component is centred at a BE of (284.8 ± 0.1) eV and is usually ascribed to the graphitic-like C–C bond, while the other two components, at (286.3 ± 0.1) and (288.9 ± 0.1) eV, are ascribed to C–O and C=O bonds, respectively.³³ Our XPS data for the C 1s core level are very close to those reported in the literature for carbon-doped TiO₂ NPs,^{33–35} in which the peaks ascribed to C–O and C=O bonds were assigned to an arylcarboxylate group, whilst the peak centred at 286.3 eV was assigned to a bidentately-bound arylcarboxylate. Thus, by analogy with those literature reports, we assigned the C 1s core level to an aromatic carbon compound.

Moreover, Zhang *et al.*³³ recently performed ion etching on similar samples in order to remove the adsorbed surface species, and access the bulk composition. XPS spectra obtained after having followed the same approach on our samples are presented in the upper panel of Fig. 4 (red spectra). The O 1s core level is very similar to the spectrum obtained before the ion etching, but an important change appears in the Ti 2p_{3/2} core level. In this peak, the main component is still related to the Ti⁴⁺ atoms of TiO₂ (see Fig. 4a), while the new small and broad component near 457.1 eV is ascribed to Ti³⁺ from the formation of oxygen vacancies induced by the ion bombardment.³³ Likewise, the C 1s core level was fitted by the same three components discussed above but, interestingly, the intensity of the signal significantly diminished. Furthermore, Fig. S5† shows a comparison of the normalised C 1s spectra before and after the ion etching. The shape, BEs and relative intensities of the main features are virtually the same before and after the erosion with argon ions. This indicates that, even after having partially cleaned the surface of the NPs, “new” carbon species inside the bulk of the TiO₂ NPs do not appear. Thus, this effect suggests a preferential covering of the surface of the NPs with carbon species, rather than their accommodation inside the TiO₂ lattice (neither interstitial nor substitutional).

Photocatalytic NO_x abatement

It is well-established that the reaction path for NO_x abatement is mediated by OH[•] radicals, and HNO₃ is generated, according to:



Such HNO₃ is produced on the surface of the catalyst, and might act as a physical barrier, inhibiting the photocatalytic reaction. As a consequence, a plateau is generally observed in

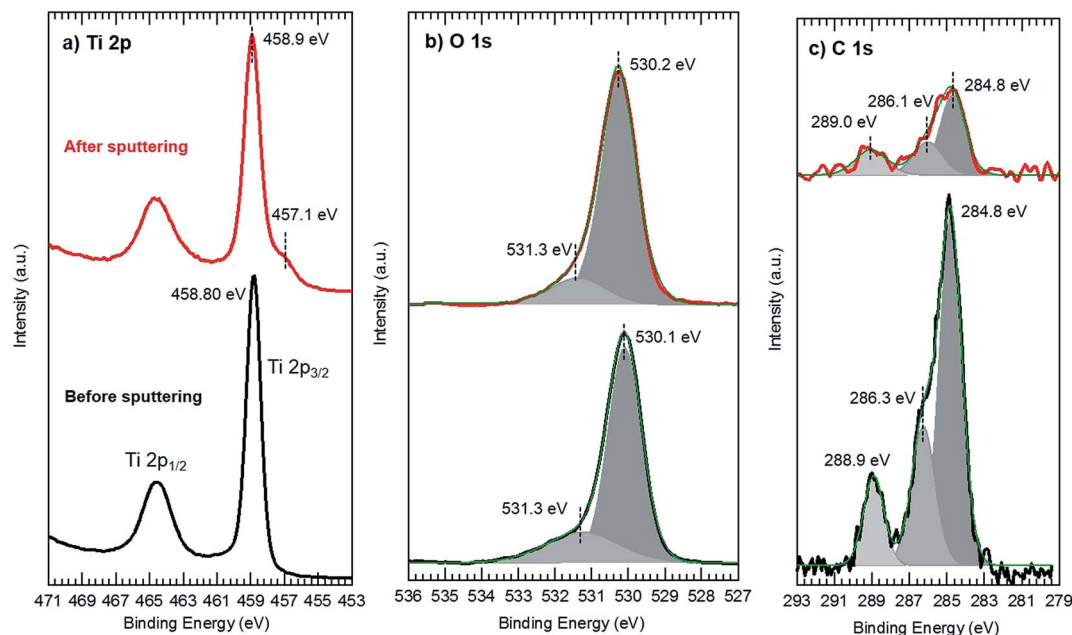


Fig. 4 High resolution XPS of Ti 2p (a), O 1s (b) and C 1s (c) core levels of the as received samples (bottom spectra in black) and after ion etching (upper spectra in red).

the NO_x abatement vs. time curve.^{36,37} This explains why the PCA tests were carried out for up to 20 min visible-light irradiation time. Nevertheless, a test up to 100 min visible-light irradiation time was assessed, and is depicted in Fig. S6.† In this, it is shown that the photocatalytic NO_x abatement is attenuated at ~ 40 min reaction time, and after this the photocatalytic reaction proceeds slowly. This likely means that the product of the photocatalytic NO_x reaction is insufficient to act as a barrier that can “deactivate” the photocatalyst – in any case, the formed HNO_3 can be easily eluted from TiO_2 into water.³⁸

NO_x abatement PCA results are shown in Fig. 5. It is seen that, in the first photocatalytic run, after 20 min reaction time the NO_x degradation by all the three batches is in the range of 20–23%. Furthermore, these PCA tests with **K7000** were shown to be repeatable, the PCA in the second and third tests being approximately the same as in the first run. This clearly shows that a complete reuse cycle is possible for **K7000**, which proved to be very stable after three consecutive photocatalytic runs for all the three batches used, and suitable for continued reuse. Also, **K7000** was shown to possess a considerably higher PCA ($\sim 30\%$ higher) compared to the well-known **P25**, under white (visible-only) indoor light (Fig. 5).

Such a superior, and very stable, PCA under white-light exposure in **K7000** has been attributed to the presence of an organic sensitizer (*i.e.* aryl carboxylate species), *cf.* spectroscopic and XPS sections, as suggested in the literature.^{33–35} Interestingly, these species clearly seem to be photostable, and thus resistant to photodegradation, which explains the stability and reusability of **K7000** (in all the three batches) when using white-light. Also, the much higher specific surface area (SSA) of **K7000** compared to that of **P25** (229.2 versus ~ 50 m^2 g^{-1} ,

respectively) and, consequently, its smaller crystalline domain size, could account for its higher PCA with regards to that of **P25** – high SSA is actually connected to a high number of active centres on the photocatalyst’s surface.³⁹ Furthermore, although we do not have any experimental evidence that upon visible-light irradiation **K7000** exhibits a better charge separation/transfer, it has been recently reported that carbon-modified TiO_2 shows improved charge separation and transfer ability.^{40,41} These findings would make **K7000** a more consistent commercial standard for comparing the indoor PCA of materials made only of the anatase TiO_2 phase.

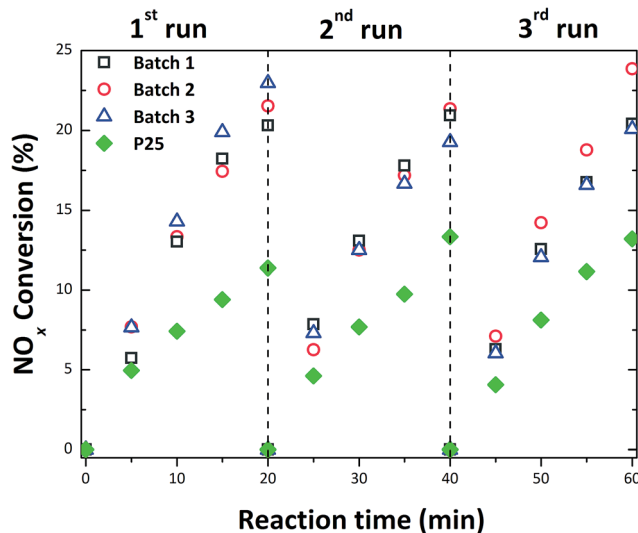


Fig. 5 Photocatalytic NO_x abatement test in triplicate of the three **K7000** batches, and **P25** as comparison, using the white LED lamp.

Conclusions

A commercial carbon-modified nano-anatase photocatalyst, KRONOClean 7000®, was characterised *via* advanced X-ray methods. Results showed the only crystalline phase to be anatase, with amorphous phase content between 6.5–8.1 wt%. They also highlighted the bimodal nature of **K7000**, with a bimodal size distribution of anatase crystalline domains in all three batches studied. This consisted of a smaller fraction of large anatase domains (11.9–15.5 nm), co-existing with a much larger quantity of smaller domains between 3.8 and 4.4 nm. XPS analysis was in agreement with results previously reported in the literature, *i.e.* that an aromatic compound was at the origin of the visible-light absorption seen in the UV-Vis spectrum.

PCA of the commercial material (in three batches) was assessed against NO_x abatement, simulating an indoor environment (pollutant concentration, and intensity of the white-light entering the reactor). It was found that the **K7000** photocatalyst showed a higher PCA (~30% higher) compared to that of the well-known **P25**. Furthermore, **K7000** exhibited a very stable PCA after three consecutive photocatalytic runs, and proved suitable for reuse. **K7000** is highlighted as a promising commercial anatase standard for indoor (visible-light) PCA applications.

Acknowledgements

Authors are grateful to the ECO-SEE project (European Union's Seventh Framework Programme funding, grant agreement no 609234). This work was developed in the scope of the project CICECO – Aveiro Institute of Materials (Ref. FCT UID/CTM/50011/2013), financed by national funds through the FCT/MEC and when applicable co-financed by FEDER under the PT2020 Partnership Agreement. R. C. Pullar acknowledges the support of FCT grant SFRH/BPD/97115/2013. M. Ferro and RNME – University of Aveiro, FCT Project REDE/1509/RME/2005 – are kindly acknowledged for HR-TEM analysis. Dr C. Scherer (Fraunhofer-Institut für Bauphysik, Germany) is kindly acknowledged for his helpful discussion. G. Otero-Irurueta would like to thank FCT from Portugal for his Post-Doctoral research grant (SFRH/BPD/90562/2012).

Notes and references

- 1 A. Fujishima and K. Honda, *Nature*, 1972, **238**, 37–38.
- 2 P. V. Kamat, *J. Phys. Chem. Lett.*, 2011, **2**, 839–840.
- 3 X. Chen and A. Selloni, *Chem. Rev.*, 2014, **114**, 9281–9282.
- 4 Y. Zhang, Z.-R. Tang, X. Fu and Y.-J. Xu, *Appl. Catal., B*, 2011, **106**, 445–452.
- 5 S. Liu, Z.-R. Tang, Y. Sun, J. C. Colmenares and Y.-J. Xu, *Chem. Soc. Rev.*, 2015, **44**, 5053–5075.
- 6 N. Zhang, M.-Q. Yang, S. Liu, Y. Sun and Y.-J. Xu, *Chem. Rev.*, 2015, **115**, 10307–10377.
- 7 Z. Şen, *Solar energy fundamentals and modeling techniques: atmosphere, environment, climate change, and renewable energy*, Springer, London, 2008.
- 8 S.-D. Mo and W. Y. Ching, *Phys. Rev. B: Condens. Matter Mater. Phys.*, 1995, **51**, 13023–13032.
- 9 R. Asahi, T. Morikawa, T. Ohwaki, K. Aoki and Y. Taga, *Science*, 2001, **293**, 269–271.
- 10 D. M. Tobaldi, C. Piccirillo, R. C. Pullar, A. F. Gualtieri, M. P. Seabra, P. M. L. Castro and J. A. Labrincha, *J. Phys. Chem. C*, 2014, **118**, 4751–4766.
- 11 D. M. Tobaldi, R. C. Pullar, A. S. Škapin, M. P. Seabra and J. A. Labrincha, *Mater. Res. Bull.*, 2014, **50**, 183–190.
- 12 D. M. Tobaldi, R. C. Pullar, M. P. Seabra and J. A. Labrincha, *Mater. Lett.*, 2014, **122**, 345–347.
- 13 D. C. Hurum, A. G. Agrios, K. A. Gray, T. Rajh and M. C. Thurnauer, *J. Phys. Chem. B*, 2003, **107**, 4545–4549.
- 14 D. O. Scanlon, C. W. Dunnill, J. Buckeridge, S. A. Shevlin, A. J. Logsdail, S. M. Woodley, C. R. A. Catlow, M. J. Powell, R. G. Palgrave, I. P. Parkin, G. W. Watson, T. W. Keal, P. Sherwood, A. Walsh and A. A. Sokol, *Nat. Mater.*, 2013, **12**, 798–801.
- 15 A. F. Gualtieri, *J. Appl. Crystallogr.*, 2000, **33**, 267–278.
- 16 A. C. Larson and R. B. von Dreele, *General Structure Analysis System (GSAS)*, Los Alamos National Laboratory Report LAUR, 2004.
- 17 B. H. Toby, *J. Appl. Crystallogr.*, 2001, **34**, 210–213.
- 18 P. Scardi and M. Leoni, *Acta Crystallogr., Sect. A: Found. Crystallogr.*, 2002, **58**, 190–200.
- 19 *Diffraction Analysis of the Microstructure of Materials*, ed. E. J. Mittemeijer and P. Scardi, Springer, 2004th edn, 2004.
- 20 M. Leoni, T. Confente and P. Scardi, *Z. Geomorphol., Suppl.*, 2006, **23**, 249–254.
- 21 G. Caglioti, A. Paoletti and F. P. Ricci, *Nucl. Instrum. Methods*, 1960, **9**, 195–198.
- 22 D. M. Tobaldi, R. C. Pullar, R. Binions, A. Belen Jorge, P. F. McMillan, M. Saeli, M. P. Seabra and J. A. Labrincha, *Catal. Sci. Technol.*, 2014, **4**, 2134.
- 23 D. M. Tobaldi, R. a. S. Ferreira, R. C. Pullar, M. P. Seabra, L. D. Carlos and J. A. Labrincha, *J. Mater. Chem. C*, 2015, **3**, 4970–4986.
- 24 U. I. Gaya and A. H. Abdullah, *J. Photochem. Photobiol., C*, 2008, **9**, 1–12.
- 25 R. Quesada-Cabrera, A. Mills and C. O'Rourke, *Appl. Catal., B*, 2014, **150–151**, 338–344.
- 26 <http://kronostio2.com/en/component/jdownloads/finish/99/288>, accessed October 2015.
- 27 V. N. Kuznetsov and N. Serpone, *J. Phys. Chem. C*, 2009, **113**, 15110–15123.
- 28 F. Spadavecchia, G. Cappelletti, S. Ardizzzone, C. L. Bianchi, S. Cappelli, C. Oliva, P. Scardi, M. Leoni and P. Fermo, *Appl. Catal., B*, 2010, **96**, 314–322.
- 29 N. Serpone, D. Lawless and R. Khairutdinov, *J. Phys. Chem.*, 1995, **99**, 16646–16654.
- 30 X. Xue, W. Ji, Z. Mao, H. Mao, Y. Wang, X. Wang, W. Ruan, B. Zhao and J. R. Lombardi, *J. Phys. Chem. C*, 2012, **116**, 8792–8797.
- 31 G. Balasubramanian, D. D. Dionysiou, M. T. Suidan, I. Baudin and J.-M. L ain e, *Appl. Catal., B*, 2004, **47**, 73–84.

- 32 D. M. Tobaldi, R. C. Pullar, A. F. Gualtieri, G. Otero-Irurueta, M. K. Singh, M. P. Seabra and J. A. Labrincha, *J. Solid State Chem.*, 2015, **231**, 87–100.
- 33 L. Zhang, M. S. Tse, O. K. Tan, Y. X. Wang and M. Han, *J. Mater. Chem. A*, 2013, **1**, 4497.
- 34 P. Ząbek, J. Eberl and H. Kisch, *Photochem. Photobiol. Sci.*, 2009, **8**, 264–269.
- 35 J. Zhuang, Q. Tian, H. Zhou, Q. Liu, P. Liu and H. Zhong, *J. Mater. Chem.*, 2012, **22**, 7036.
- 36 J. Lasek, Y.-H. Yu and J. C. S. Wu, *J. Photochem. Photobiol., C*, 2013, **14**, 29–52.
- 37 Y. Ohko, Y. Nakamura, A. Fukuda, S. Matsuzawa and K. Takeuchi, *J. Phys. Chem. C*, 2008, **112**, 10502–10508.
- 38 T. Ibusuki and K. Takeuchi, *J. Mol. Catal.*, 1994, **88**, 93–102.
- 39 K. A. Michalow, D. Logvinovich, A. Weidenkaff, M. Amberg, G. Fortunato, A. Heel, T. Graule and M. Rekas, *Catal. Today*, 2009, **144**, 7–12.
- 40 Y. Zhang, Z.-R. Tang, X. Fu and Y.-J. Xu, *ACS Nano*, 2010, **4**, 7303–7314.
- 41 J. Su, P. Geng, X. Li, Q. Zhao, X. Quan and G. Chen, *Nanoscale*, 2015, **7**, 16282–16289.